

Article

Cathodic and Anodic Stress Corrosion Cracking of a New High-Strength CrNiMnMoN Austenitic Stainless Steel

Mathias Truschner ^{1,*} , Jacqueline Deutsch ¹, Gregor Mori ¹ and Andreas Keplinger ²

¹ Chair of General and Analytical Chemistry, Montanuniversitaet Leoben, 8700 Leoben, Austria; jacqueline.deutsch@unileoben.ac.at (J.D.); gregor.mori@unileoben.ac.at (G.M.)

² Voestalpine BOHLER Edelstahl GmbH and Co KG, 8605 Kapfenberg, Austria; andreas.keplinger@bohler-edelstahl.at

* Correspondence: mathias.truschner@unileoben.ac.at; Tel.: +43-650-6343-358

Received: 29 October 2020; Accepted: 13 November 2020; Published: 19 November 2020



Abstract: A new high-nitrogen austenitic stainless steel with excellent mechanical properties was tested for its resistance to stress corrosion cracking. The new conventional produced hybrid CrNiMnMoN stainless steel combines the excellent mechanical properties of CrMnN stainless steels with the good corrosion properties of CrNiMo stainless steels. Possible applications of such a high-strength material are wires in maritime environments. In principle, the material can come into direct contact with high chloride solutions as well as low pH containing media. The resistance against chloride-induced stress corrosion cracking was determined by slow strain rate tests and constant load tests in different chloride-containing solutions at elevated temperatures. Resistance to hydrogen-induced stress corrosion cracking was investigated by precharging and ongoing in-situ hydrogen charging in both slow strain rate test and constant load test. The hydrogen charging was carried out by cathodic charging in 3.5 wt.% NaCl solution with addition of 1 g/L thiourea as corrosion inhibitor and recombination inhibitor to ensure hydrogen absorption with negligible corrosive attack. Slow strain rate tests only lead to hydrogen induced stress corrosion cracking by in-situ charging, which leads to total hydrogen contents of more than 10 wt.-ppm and not by precharging alone. Excellent resistance to chloride-induced stress corrosion cracking in 43 wt.% CaCl₂ at 120 °C and in 5 wt.% NaCl buffered pH 3.5 solution at 80 °C is obtained for the investigated austenitic stainless steel.

Keywords: stress corrosion cracking; austenitic stainless steel; hydrogen-induced stress corrosion cracking; chloride-induced stress corrosion cracking

1. Introduction

Highest strength combined with excellent corrosion resistance are key requirements for most applications in the oil and gas industry. Nevertheless, there is an increased susceptibility to hydrogen induced stress corrosion cracking (HISCC) and chloride-induced stress corrosion cracking (Cl-SCC) with increasing strength [1]. For this reason, established alloying concepts today are mostly limited to CrMnN steels and CrNiMo steels. CrMnN stainless steels alloys usually achieve excellent mechanical properties through solubility hardening, but are known to be susceptible to hydrogen embrittlement (HE) and stress corrosion cracking (SCC) [2]. CrNiMo stainless steels show excellent resistance to hydrogen embrittlement and to stress corrosion cracking, but they often do not have adequate mechanical properties. Some unstable austenitic stainless steels show strain-induced martensite formation at increased plastic deformation, which again leads to increased susceptibility to hydrogen embrittlement [3]. This paper deals with the resistance of a new hybrid CrNiMnMoN stainless steel

that combines the excellent mechanical properties of CrMnN stainless steels with the good corrosion properties of CrNiMo stainless steels. Cr, Mo and N provide the corrosion resistance to pitting and crevice corrosion, Ni increases the resistance to Cl⁻SCC. Mn is used to increase strength and nitrogen solubility and N provides additional strength.

To determine the resistance to hydrogen embrittlement and stress corrosion cracking, slow strain rate tests (SSRTs) [4–6] and constant load tests (CLTs) [7,8] are mostly used. It is only by determining characteristic values from both tests that the resistance of the material can be sufficiently characterized [7,9]. Resistance to hydrogen embrittlement is in most cases achieved by testing samples pre-charged or in-situ charged with hydrogen at room temperature. Pre-loading leads to a constant level of hydrogen when the correct charging method is used, but also to hydrogen effusion during mechanical loading. In-situ charging, on the other hand, leads to an increase in the hydrogen content of the sample during the test [10,11]. Alternative methods used are the electrolytic coating of charged samples with cadmium [6] or zinc [7] to stop hydrogen effusion. However, this results in an accumulation at the interface between metal and coating. The resistance to anodic stress corrosion cracking of stainless steels is proven at higher temperatures and in more aggressive media.

From the point of view of possible damage areas of stainless steels, two categories can be roughly divided. On the one hand, damage caused by hydrogen in the cathodic potential range (HE or HISCC) and damage caused by corrosion in the anodic potential range (SCC or Cl⁻SCC) [9,12–15].

In the case of HISCC, damage is caused by hydrogen, which in most cases is formed on the metal surface by electrochemical processes and diffuses to the crack tip under tensile stress. Fundamental mechanisms which explain the damage are the hydrogen enhanced localized plasticity (HELP), hydrogen enhanced decohesion embrittlement (HEDE), adsorption induced dislocation emission (AIDE). Lynch describes prerequisites, strengths and weaknesses of each mechanism very detailed in [16].

In contrast to carbon steels, austenitic stainless steels show a much better resistance to HISCC. This is mainly due to their face-centred cubic lattice, which has a higher solubility for hydrogen and consequently a lower diffusion coefficient of hydrogen in the lattice. New studies underline the effect of microstructure on HISCC resistance. Martensitic and duplex stainless steels are more susceptible than austenitic stainless steels [17–19]. The martensitic lattice is highly stressed and has a lower solubility for hydrogen and a ferritic-austenitic mixed lattice has the problem of high solubility in the austenitic phase and the ferritic phase is in direct contact with high hydrogen concentrations at phase boundaries. As a result, the threshold hydrogen contents for HISCC of high-strength carbon steels are in the range of 1–3 wt.-ppm [20–22]. Hydrogen threshold values for austenitic stainless steels are usually between 10 and 50 wt.-ppm, whereas the values for martensitic and duplex stainless steels can be significantly lower [3,11,23].

On the other hand, anodic stress corrosion cracking can occur at the boundaries of the passive area, with the most common type of damage occurring near or at the pitting corrosion potential due to the presence of chloride ions. Material damage at such potentials is usually caused by localized corrosive attack of slip steps, while repassivation is strongly limited, and by additional hydrogen formation at the cathodic areas of the local corrosion element. The recognised damage mechanism is the slip dissolution model, where the preferred metal dissolution occurs in bare slip steps [24]. Further special forms of SCC are caused by pitting and acidification of the hole bottom and crack initiation of sensitised stainless steels as a result of intergranular attack, which is known as intergranular stress corrosion cracking (IGSCC) [25].

The aim of this work is to characterise the resistance to HISCC and Cl⁻SCC of a new high-strength, highly corrosion resistant CrNiMnMoN stainless steel and to point out the importance of material testing in the cathodic and anodic potential range.

2. Materials and Methods

A high-nitrogen austenitic stainless steel was used for the tests. The material was melted in an electric arc furnace, cast into billets, hot rolled into 9 mm diameter wire and then cooled in air. Small tensile test specimens with a diameter of 3 mm and a gauge length of 25.4 mm (Figure 1) and samples with $30 \times 6 \times 6$ mm in the form of a cuboid were eroded and machined from the wire material.

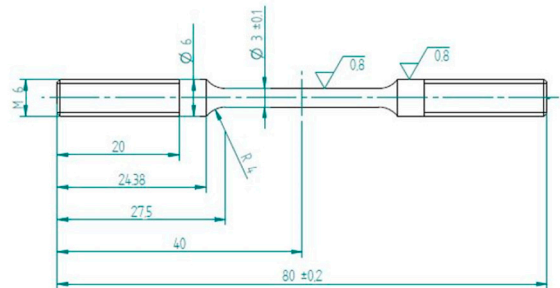


Figure 1. Tensile test sample. All measurements in mm, roughness in μm .

The surface finish of all samples used in the tests were as machined and cleaning was performed by ultrasonic cleaning in acetone twice for five minutes each time. The investigated material is a low carbon austenitic stainless steel X3CrNiMnMoN27-14-6-3 with a nitrogen content of 0.7 wt.%. The hydrogen content in the base material is 3.76 wt.-ppm and was measured with hot carrier gas extraction in a conductivity cell at 950 °C.

The ultimate tensile strength is 1050 MPa and the yield strength is 620 MPa. Microstructure after polishing and electrolytic etching in 10 wt.% oxalic acid is shown in Figure 2. The material is fully austenitic with an average grain size of approximately 15 μm . The pitting resistant equivalent number (PREN) of the material says that it is a superaustenitic stainless steel with PREN 48.1 [26,27].

$$\text{PREN} = \text{wt.\% Cr} + 3.3 \text{ wt.\% Mo} + 16 \text{ wt.\% N} \quad (1)$$

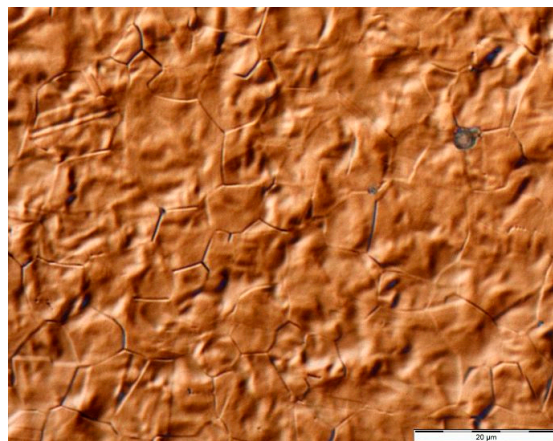


Figure 2. Microstructure after electrolytic etching in 10 wt.% oxalic acid.

The critical pitting temperature in 6 wt.% FeCl_3 plus 1 wt.% HCl according to the ASTM G48 method C was measured to be above 90 °C.

2.1. Hydrogen Charging

The hydrogen charging serves as a partial step to determine the resistance to HISCC. The samples were cathodically charged under the following conditions (Table 1).

Table 1. Hydrogen Charging Conditions.

Medium	Thiourea (g/L)	Current Density (mA/cm ²)	Temperature (°C)
3.5 wt.% NaCl	1	1	23
3.5 wt.% NaCl	1	10	23

Cathodic charging is the most effective way to achieve an appropriate amount of hydrogen in austenitic steels when testing against HISSC [11,28]. Thiourea acts both as a recombination inhibitor and as a corrosion inhibitor and thus brings the effect of increased hydrogen absorption, but also of reduced corrosion attack. The total hydrogen content was determined by carrier gas hot extraction in a thermal conductivity cell at 950 °C. Two different current densities were selected to achieve different hydrogen contents and to set a possible saturation, the respective experiments were carried out for different times.

2.2. SSRT

The SSRT test is used as an accelerated test method to determine the properties of a material against HISSC and Cl⁻SCC. When using SSRT, it is important to select the strain rate within a certain range, as there can be drastic influences on the measurement results due to various mostly diffusion-controlled processes. Kim and Wilde [29] have shown in their work that SCC only occurs at medium strain rates and HISSC occurs at medium to low strain rates. The selected test conditions should reflect damage areas of stainless steels of practical relevance. The conditions for HISSC were chosen to test hydrogen contents in the range of the threshold concentrations from literature, while the conditions for Cl⁻SCC reflect test media with increasingly aggressive conditions, which are relevant for example in the oil and gas production (Table 2).

Table 2. SSRT Conditions.

Medium	Precharging	Strain Rate (1/s)	Temperature (°C)
Air	1 mA/cm ² , 3 days	2 × 10 ⁻⁶	23
3.5 wt.% NaCl + 1 g/L CH ₄ N ₂ S	1 mA/cm ² , 3 days	2 × 10 ⁻⁶	23
3.5 wt.% NaCl + 1 g/L CH ₄ N ₂ S	10 mA/cm ² , 3 days	2 × 10 ⁻⁶	23
Buffered 5 wt.% NaCl, pH 3.5	No	2 × 10 ⁻⁶	80
43 wt.% CaCl ₂	No	2 × 10 ⁻⁶	120
42 wt.% MgCl ₂	No	2 × 10 ⁻⁶	120

To provide comparative values, SSRTs were additionally performed in air at room temperature (RT) and in glycerine at 80 and 120 °C. SSRTs were performed on a universal testing machine of type Beta RV. For the HISSC tests in-situ hydrogen charging was used with a constant current density using a platinum mesh as counter electrode. For the Cl⁻SCC measurements at open circuit potential the chloride solution temperature was controlled by a heated double walled vessel with an external thermometer and water cooling was used to prevent the test medium from evaporating.

The SCC susceptibility index can be calculated by the elongation ratio (RE), which compares elongation under inert conditions (E_i) with elongation in the aggressive environment (E_a),

$$\text{Elongation Ratio RE} = E_i/E_a \quad (2)$$

or by the reduction in area ratio (RRA) (ratio of reduction in area under inert conditions (RA_i), divided by reduction of area in the aggressive environment (RA_a), which can be described as followed:

$$\text{Reduction of Area Ratio RRA} = RA_i/RA_a \quad (3)$$

2.3. CLT

CLTs are used to determine threshold stresses, which have more practical relevance than SSRTs, but are much more time consuming than SSRTs. These tests are carried out under constant load at a certain percentage of the yield strength, thus producing a condition that comes close to reality. However, the test duration is much longer than the SSRT tests and therefore only a few selected media were investigated (Table 3). The limit time was chosen to be 510 h, as it can be assumed that breaking only occurs in this time range and for longer times material can be called resistant to SCC. Different test stresses were applied at 80, 100 and 120% of the YS each.

Table 3. CLT Conditions.

Medium	Precharging	Temperature (°C)
3.5 wt.% NaCl + 1 g/L CH ₄ N ₂ S	10 mA/cm ² , 3 days	23
Buffered 5 wt.% NaCl, pH 3.5	No	80
42 wt.% MgCl ₂	No	120

CLTs were performed on a lever apparatus with the same glass cells as described in Section 2.2. The applied force was measured by a load cell before each test. The CLTs were monitored with a time lapse camera. One image per hour of testing time was made and the time to failure was determined by evaluation of the camera images, whereby the last image on which the sample has not yet broken plus half an hour was taken as time to failure to achieve an accuracy of 30 min.

3. Results

3.1. Hydrogen Charging

Figure 3 shows the total hydrogen content after different charging times. After 7 days, a plateau value is reached, which increases only slightly after longer periods. With increased current density, higher hydrogen contents can be reached. After evaluation of several reference samples, it can be seen that there are greater deviations at higher hydrogen contents and, therefore, the scattering bars are given with 5%.

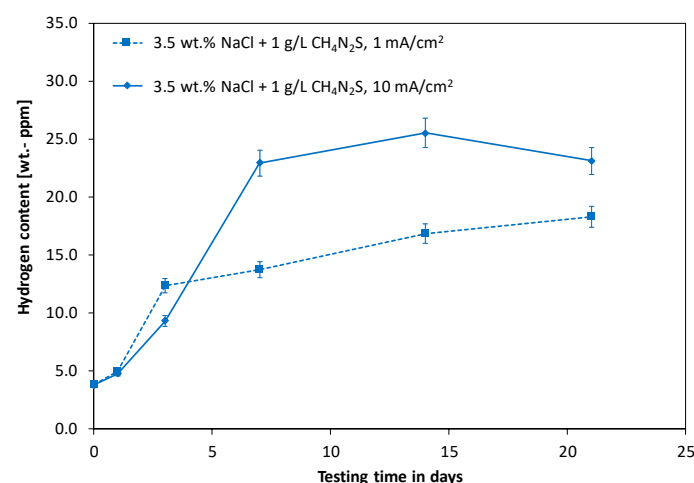


Figure 3. Hydrogen charging results for two different current densities, both at room temperature.

3.2. SSRT

The SSRT results of the hydrogen charged and the inert conditions are shown in Figure 4. The test at an in-situ charging current density of 1 mA/cm² shows an embrittlement index of 0.85 for the

elongation value and 0.86 for the reduction in area value and at a magnification of 6 clearly recognizable HISCC indicated by additional cracks parallel to the fracture surface and a reduced reduction of area (Figure 4b) compared to the inert conditions (Figure 4a). A more pronounced behaviour can be seen at an increased current density, with an embrittlement index of 0.65 for RE and 0.43 for RRA, while the sample without in-situ charging does not show any embrittlement.

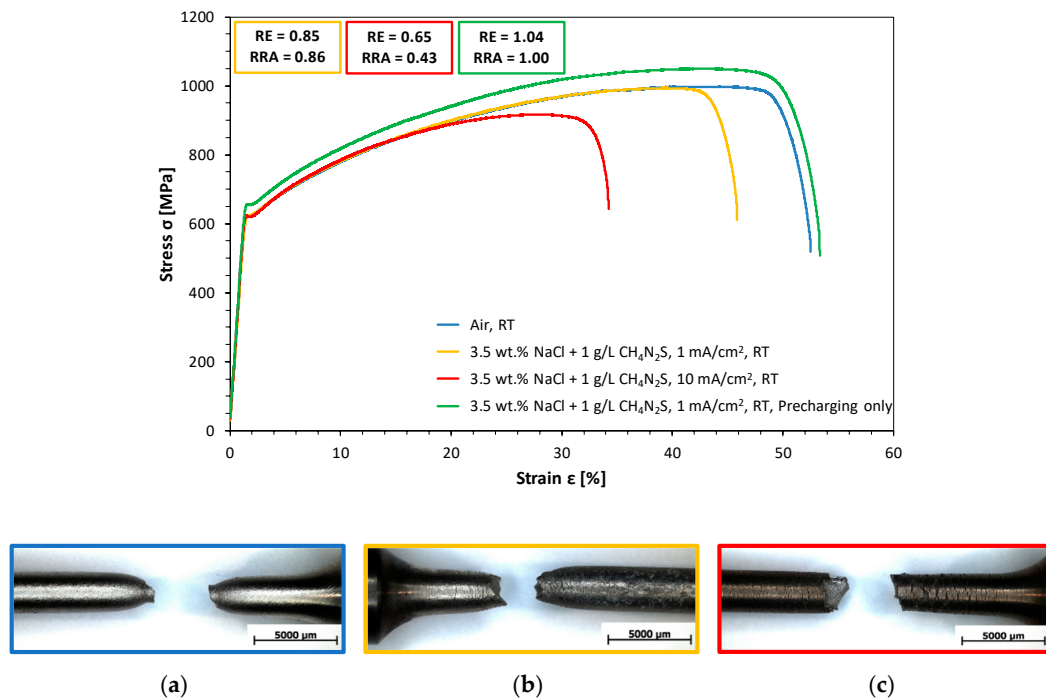


Figure 4. HISCC results for different charging methods and optical microscopy of selected samples after SSRT testing: (a) Air, RT (b) 3.5 wt.% NaCl + 1 g/L CH₄N₂S, 1 mA/cm², RT (c) 3.5 wt.% NaCl + 1 g/L CH₄N₂S, 10 mA/cm², RT.

In Figures 5 and 6, the fracture surfaces of the air-tested and the hydrogen-charged specimen are compared. The air sample shows a ductile behaviour over the whole fracture surface, evident from the characteristic dimples. The SSRT with in-situ hydrogen charging led to cracks from the outside to the centre of the sample. The fracture surface can therefore be divided into three main parts of hydrogen attack. First, a brittle part near the surface of the sample with mainly transgranular hydrogen induced cracks (Figure 6b,c). In the centre of the sample there is a part with flat and regular dimples, which is also intended to be a hydrogen effect coming from lower hydrogen concentrations (Figure 6f) and in between the transition zone (Figure 6e).

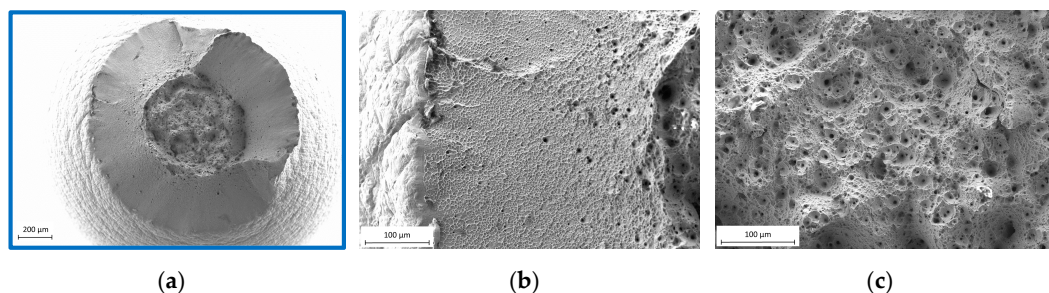


Figure 5. Fracture surface of the SSRT in air at room temperature without hydrogen charging: (a) ductile fracture appearance over the whole surface, (b) dimple structure at the edge of the sample, with clearly visible lines of deformation on the outer surface of the sample, (c) pure ductile structure in the center of the sample.

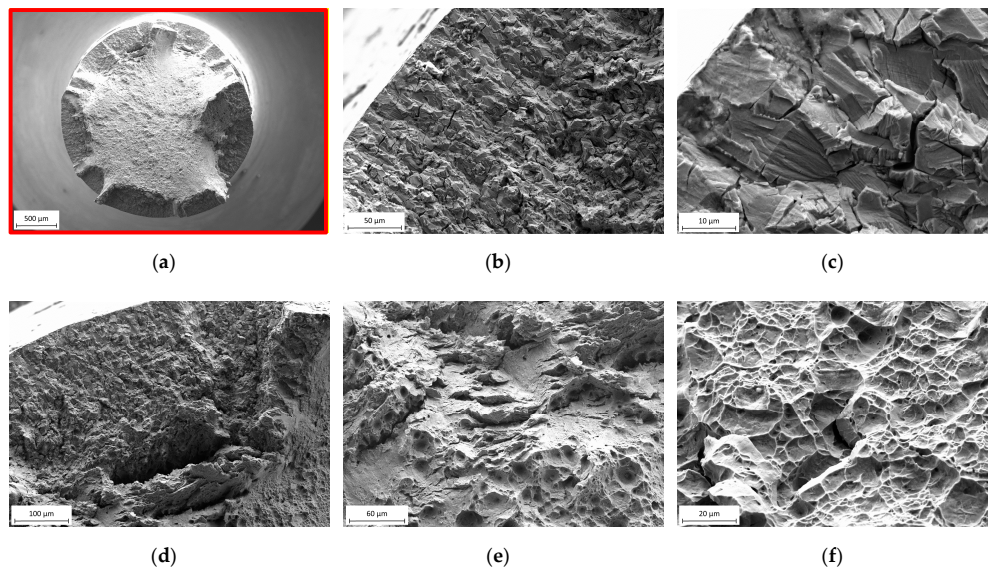


Figure 6. Fracture surface of the 10 mA/cm² in-situ hydrogen charged SSRT at room temperature: (a) markedly reduced reduction in area and visible cracks from the surface to the centre, (b) hydrogen induced cracking at the edge of the sample, (c) transgranular cracking with minor amounts of intergranular cracks, (d) transitions from the hydrogen induced cracking to a more ductile part in the centre of the sample, (e) transition zone between hydrogen induced cracking and ductile fracture with some dimples, (f) flat dimples in the centre of the sample.

Looking at the SSRT results in Figure 7, best resistance can be seen in 43 wt.% CaCl₂, at 120 °C and in a buffered 5 wt.% NaCl solution with pH 3.5 at 80 °C. In these two cases, no Cl⁻SCC can be seen stereomicroscopically and the embrittlement index is higher than 0.8, which means hardly any embrittlement. Significant embrittlement occurs when testing the material in 42 wt.% MgCl₂ at 120 °C. Clear Cl⁻SCC can be seen and the embrittlement index is below 0.2, which means a high susceptibility to SCC in this environment.

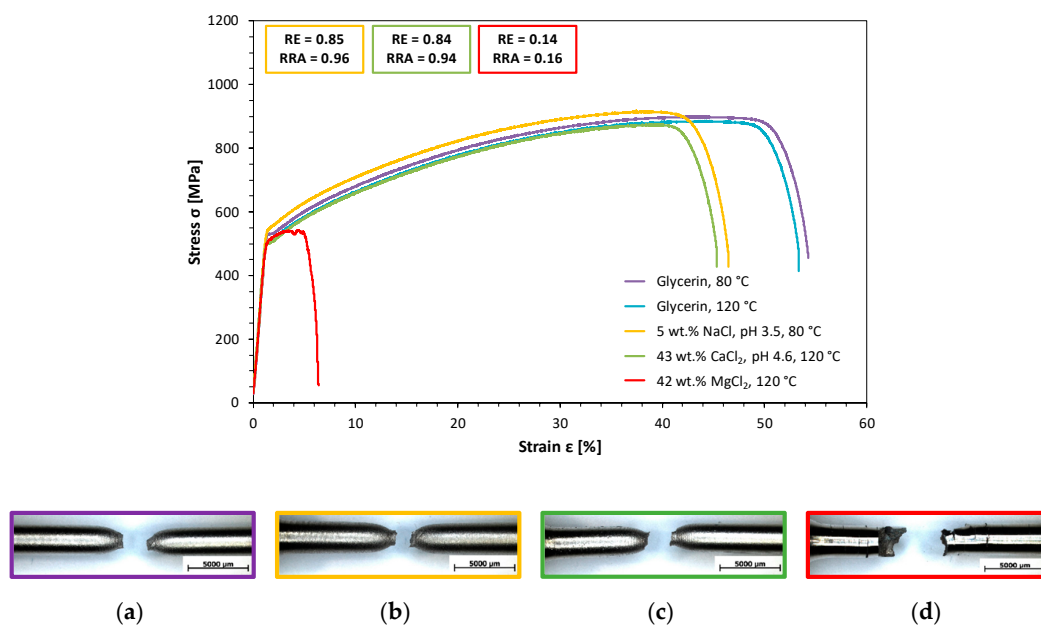


Figure 7. Cl⁻SCC results for different solutions and optical microscopy of selected samples after SSRT testing: (a) Glycerine, 120 °C, (b) 5 wt.% NaCl pH 3.5, 80 °C, (c) 43 wt.% CaCl₂, 120 °C, (d) 42 wt.% MgCl₂, 120 °C.

The fracture surfaces of the Cl⁻SCC samples are shown in Figures 8–11. The fracture surface of the SSRT in the buffered 5 wt.% NaCl solution at 80 °C and the SSRT in the 43 wt.% CaCl₂ solution at 120 °C show very similar behaviour as the inert sample. All three fracture surfaces show deformation lines on the outer surface and a characteristic dimple structure over the whole fracture surface. Clearly recognizable SCC only occurs in MgCl₂ at 120 °C, which leads to mainly intergranular cracks at the edge of the sample and to both inter- and transgranular cracks in the centre of the sample.

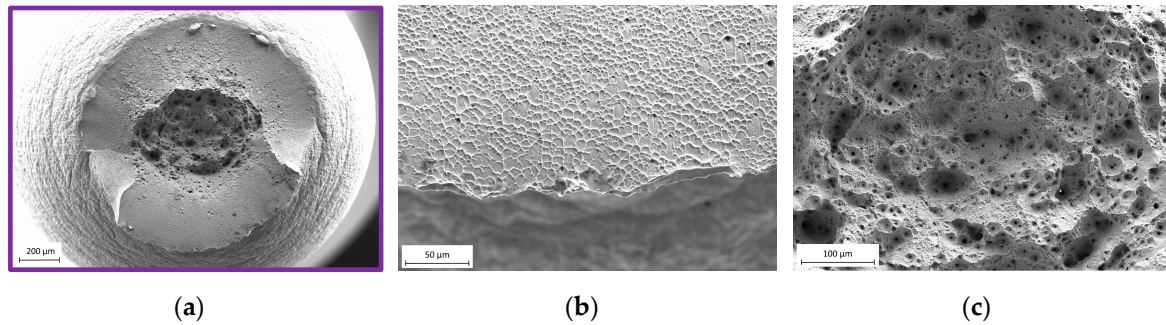


Figure 8. Fracture surface of the inert SSRT at 80 °C: (a) ductile appearance over the whole fracture surface and visible deformation lines on the outer surface of the sample, (b) pure ductile structure at the edge of the sample, (c) deep dimples at the centre of the fracture surface.

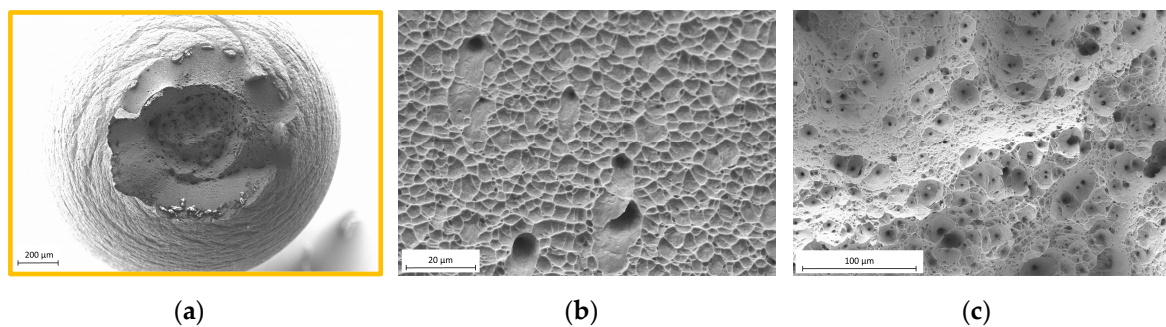


Figure 9. Fracture surface of the SSRT in 5 wt.% NaCl buffered to pH 3.5 at 80 °C: (a) pure ductile fracture surface without visible cracking, (b) ductile structure at the edge of the sample, (c) ductile dimples in the centre of the sample.

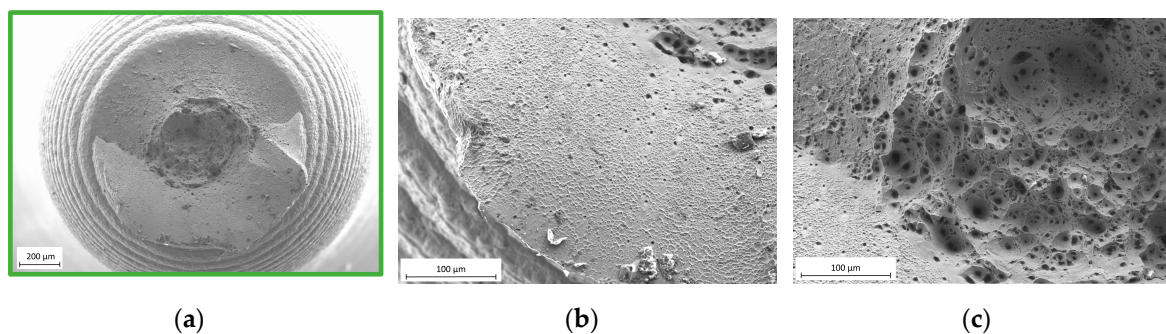


Figure 10. Fracture surface of the SSRT in 43 wt.% CaCl₂ at 120 °C: (a) no visible Cl⁻SCC at the fracture surface, (b) ductile structure at the edge of the sample, (c) dimple structure at the centre of the sample without visible cracks.

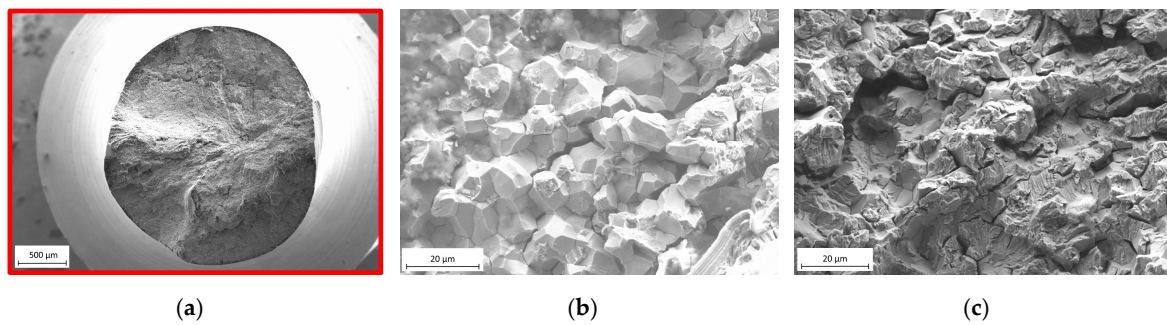


Figure 11. Fracture surface of the SSRT in 42 wt.% MgCl₂ at 120 °C: (a) markedly reduced reduction in area and visible stress corrosion cracking, (b) mainly intergranular stress corrosion cracking at the edge of the sample, (c) inter- and transgranular cracking in the centre of the sample.

3.3. CLT

The CLT with simultaneous hydrogen charging did not lead to any breakage even under the highest load ($1.2 \times YS$). Looking at the results from the CLTs at higher temperatures, no embrittlement is observed in the buffered 5 wt.% NaCl, pH 3.5 solution and in 42 wt.% MgCl₂ at 120 °C, failure only occurs at higher loads. Table 4 shows the results for the time to failure of the CLTs.

Table 4. CLT Results for HISCC and CI-SCC Conditions.

Medium	Stress (MPa)	Stress Ratio (-)	Time to Failure (h)
3.5 wt.% NaCl + 1 g/L CH ₄ N ₂ S, 10 mA/cm ² , 3 d precharging + continued charging during CLT	744	1.2	-
Buffered 5 wt.% NaCl, pH 3.5, 80 °C	439	0.8	-
	559	1.0	-
	679	1.2	-
42 wt.% MgCl ₂ , 120 °C	439	0.8	-
	559	1.0	179
	679	1.2	7

4. Conclusions

Following conclusions can be drawn from this work:

- The excellent mechanical properties of high-strength CrMnN stainless steels and high corrosion resistance of CrNiMo stainless steels can be combined by the development of CrNiMnMoN stainless steels. A new X3CrNiMnMo27-14-6-3 stainless steel was produced by conventional melting in an electric arc furnace followed by argon oxygen decarburization treatment, billet casting and hot rolling.
- Cathodic hydrogen charging in neutral solutions with the addition of thiourea leads to hydrogen values up to 25 wt.-ppm, which does not lead to failure when testing with constant load at 1.2 times the yield strength.
- SSRTs only lead to HISCC when charged in-situ with total hydrogen contents of more than 10 wt.-ppm and not by precharging alone.
- SSRTs are much more severe than CLTs for testing the resistance to HISCC.
- Excellent resistance to CI-SCC in 43 wt.% CaCl₂ at 120 °C and in 5 wt.% NaCl buffered pH 3.5 solution at 80 °C is obtained for the investigated stainless steel.
- Markedly reduced elongation and reduction in area is obtained in 42 wt.% MgCl₂ at 120 °C by inter—and transgranular SCC.

- The new X3CrNiMnMo27-14-6-3 stainless steel tolerates hydrogen contents of up to 25 wt.-ppm and can be used in 5% NaCl buffered pH 3.5 solution at 80 °C as well as in 43% CaCl₂ at 120 °C.

5. Discussion

Based on the results of the hydrogen charging, it was found that it is necessary to carry out a precharging before the start of the experiment, otherwise the SSRT would be carried out with a variable hydrogen content of the specimen. Precharging alone does not lead to embrittlement, thus confirming the assumption that in-situ hydrogen charging is much more aggressive and more suitable for performing HISCC tests. Damage only occurs with continued charging and shows the characteristic embrittlement behaviour of an austenitic material above hydrogen contents of 10 wt.-ppm [30]. In case of hydrogen embrittlement, it is particularly noticeable that there is a high degree of embrittlement at the edge, which decreases towards the centre of the sample. This can be explained by the concentration gradient of hydrogen in the material, which is predominant as a result of the low diffusion rate during in-situ hydrogen charging and has been shown earlier by Herms, Olive and Puiggali [30] for an austenitic stainless steel of type 316 L. Due to the significant embrittlement at total hydrogen contents of 25 wt.-ppm and the obvious presence of a hydrogen concentration gradient, there are significantly higher local hydrogen contents at the surface, which lead to a brittle cracking. Omura et al. [3] have published a critical surface hydrogen concentration of 2000 ppm for high-nitrogen steels.

There is no cracking or visible embrittlement after testing at a constant load, while SSRT has shown embrittlement. Consequently, under given conditions, SSRT can be considered more severe than CLT. This is due to higher stresses up to UTS during SSRT.

Because of its high Ni content, the material shows good resistance to Cl⁻SCC. Nickel contributes to the formation of fine slip steps and thus to improved repassivation behaviour [31].

The high-nitrogen content also gives the material a high resistance to pitting corrosion, which can often be a trigger for SCC [32]. Toppo et al. [33] have also shown in their work that austenitic stainless steels with high-nitrogen contents are more resistant to pitting and thus increase SCC resistance by preventing the formation of cracks starting from pits.

The threshold stress for SCC initiation determined by CLT for the high-nitrogen steel is about 500 MPa, while other austenitic stainless steels often show significantly lower threshold stresses. The X2CrNiMo18-14-3 steel, which is comparable to the familiar 316 L, shows a threshold stress of 290 MPa in 45 wt.% MgCl₂ at 120 °C [34]. Through this work it is clear that it is essential to know the areas of vulnerability of a material and to test it in those areas to ensure safe use. Resistance to stress corrosion cracking must therefore be ensured for an austenitic stainless steel not only for anodic SCC, but also for cathodic SCC due to hydrogen.

Author Contributions: Conceptualization, M.T.; Data curation, J.D.; Methodology, M.T. and J.D.; Project administration, G.M. and A.K.; Supervision, G.M.; Writing—original draft, M.T.; Writing—review and editing, G.M. and A.K. All authors have read and agreed to the published version of the manuscript.

Funding: This research received no external funding.

Acknowledgments: The authors would like to thank the project partners: voestalpine BOHLER Edelstahl GmbH & Co KG and voestalpine Wire Austria GmbH.

Conflicts of Interest: The authors declare no conflict of interest.

References

1. Trautmann, A.; Mori, G.; Oberndorfer, M.; Bauer, S.; Holzer, C.; Dittmann, C. Hydrogen Uptake and Embrittlement of Carbon Steels in Various Environments. *Materials* **2020**, *13*, 3604. [[CrossRef](#)] [[PubMed](#)]
2. Bacchi, L.; Biagini, F.; Corsinovi, S.; Romanelli, M.; Villa, M.; Valentini, R. Influence of Thermal Treatment on SCC and HE Susceptibility of Supermartensitic Stainless Steel 16Cr5NiMo. *Materials* **2020**, *13*, 1643. [[CrossRef](#)] [[PubMed](#)]

3. Omura, T.; Nakamura, J.; Hirata, H.; Jotoku, K.; Ueyama, M.; Osuki, T.; Terunuma, M. Effect of Surface Hydrogen Concentration on Hydrogen Embrittlement Properties of Stainless Steels and Ni Based Alloys. *ISIJ Int.* **2016**, *56*, 405–412. [[CrossRef](#)]
4. Tagliari, M.D.R.; Antunes, M.R.; Santos, J.G.N.D.; Santos, F.P.D.; Santos, J.M.C.D.; Falcade, T.; Reguly, A. Tensile Armor Wires Submitted to Slow Strain Rate Tests in a Corrosive Environment and Cathodic Protection: A Comparison Between Two Different Microstructures. *Mat. Res.* **2019**, *22*, 853. [[CrossRef](#)]
5. Zhong, X.; Bali, S.C.; Shoji, T. Accelerated test for evaluation of intergranular stress corrosion cracking initiation characteristics of non-sensitized 316 austenitic stainless steel in simulated pressure water reactor environment. *Corr. Sci.* **2017**, *115*, 106–117. [[CrossRef](#)]
6. Li, X.; Zhang, J.; Wang, Y.; Shen, S.; Song, X. Effect of hydrogen on tensile properties and fracture behavior of PH 13-8 Mo steel. *Mater. Des.* **2016**, *108*, 608–617. [[CrossRef](#)]
7. Chida, T.; Hagihara, Y.; Akiyama, E.; Iwanaga, K.; Takagi, S.; Hayakawa, M.; Ohishi, H.; Hirakami, D.; Tarui, T. Comparison of Constant Load, SSRT and CSRT Methods for Hydrogen Embrittlement Evaluation Using Round Bar Specimens of High Strength Steels. *ISIJ Int.* **2016**, *56*, 1268–1275. [[CrossRef](#)]
8. Trautmann, A.; Mori, G.; Siegl, W.; Truschner, M.; Pfeiffer, J.; Kapp, M.; Keplinger, A.; Oberndorfer, M.; Bauer, S. Hydrogen Uptake of Duplex 2205 at H₂ Partial Pressures up to 100 bar. *BHM Berg-Und Hüttenmännische Mon.* **2020**, *165*, 40–45. [[CrossRef](#)]
9. Shoji, T.; Raja, V.S. Stress Corrosion Cracking. In *Theory and Practice*; Woodhead Pub: Oxford, PA, USA, 2011; ISBN 9780857093769.
10. Takagi, S.; Toji, Y. Application of NH₄SCN Aqueous Solution to Hydrogen Embrittlement Resistance Evaluation of Ultra-high Strength Steels. *ISIJ Int.* **2012**, *52*, 329–331. [[CrossRef](#)]
11. Hüter, C.; Shanthraj, P.; McEniry, E.; Spatschek, R.; Hickel, T.; Tehranchi, A.; Guo, X.; Roters, F. Multiscale Modelling of Hydrogen Transport and Segregation in Polycrystalline Steels. *Metals* **2018**, *8*, 430. [[CrossRef](#)]
12. Pohjanne, P.; Vepsäläinen, M.; Saario, T.; Sipilä, K.; Romu, J.; Saukkonen, T.; Hänninen, H.; Heikkilä, M.; Koskiniemi, J.; Berg, C.-G. Effect of Electrochemical Potential on Stress Corrosion Cracking Susceptibility of EN 1.4301 (AISI 304) Austenitic Stainless Steels in Simulated Hot Black Liquor. *Corrosion* **2015**, *71*, 887–894. [[CrossRef](#)]
13. Sridhar, N.; Thodla, R.; Gui, F.; Cao, L.; Anderko, A. Corrosion-resistant alloy testing and selection for oil and gas production. *Corros. Sci. Eng. Techn.* **2018**, *53*, 75–89. [[CrossRef](#)]
14. Staehle, R.W. *Bases for Predicting the Earliest Penetrations Due to SCC for Alloy 600 on the secondary Side of PWR Steam Generators*; NUREG/CT-6737; United States Nuclear Regulatory Commission: Washington, DC, USA, 2001.
15. Landolt, D. *Corrosion and Surface Chemistry of Metals*; CRC Press: Lausanne, FL, USA, 2007; ISBN 978-0-8493-8233-8.
16. Lynch, S. Hydrogen embrittlement phenomena and mechanisms. *Corros. Rev.* **2012**, *30*, 1107. [[CrossRef](#)]
17. Świerczyńska, A.; Fydrych, D.; Landowski, M.; Rogalski, G.; Łabanowski, J. Hydrogen embrittlement of X2CrNiMoCuN25-6-3 super duplex stainless steel welded joints under cathodic protection. *Constr. Build. Mater.* **2020**, *238*, 117697. [[CrossRef](#)]
18. He, J.; Chen, L.; Tao, X.; Antonov, S.; Zhong, Y.; Su, Y. Hydrogen embrittlement behavior of 13Cr-5Ni-2Mo supermartensitic stainless steel. *Corr. Sci.* **2020**, *176*, 109046. [[CrossRef](#)]
19. Allam, T.; Guo, X.; Lipińska-Chwałek, M.; Hamada, A.; Ahmed, E.; Bleck, W. Impact of precipitates on the hydrogen embrittlement behavior of a V-alloyed medium-manganese austenitic stainless steel. *J. Mater. Res. Technol.* **2020**, *9*, 13524–13538. [[CrossRef](#)]
20. Kan, B.; Wu, W.; Yang, Z.; Li, J. Stress-induced hydrogen redistribution and corresponding fracture behavior of Q960E steel at different hydrogen content. *Mater. Sci. Eng. A* **2020**, *775*, 138963. [[CrossRef](#)]
21. Asahi, H.; Ueno, M.; Yonezawa, T. Prediction of Sulfide Stress Cracking in High-Strength Tubulars. *Corrosion* **1994**, *50*, 537–545. [[CrossRef](#)]
22. Scharf, R.; Muhr, A.; Stellnberger, K.-H.; Faderl, J.; Holzer, C.; Mori, G. Hydrogen embrittlement of high strength steel under in situ corrosive charging conditions and tensile load. *Werkst. Korros.* **2017**, *68*, 95–104. [[CrossRef](#)]
23. Lauvstad, G.Ø.; Johnsen, R.; Asbjørnsen, I.; Bjurström, M.; Hjorth, C.-G. Resistance Toward Hydrogen-Induced Stress Cracking of Hot Isostatically Pressed Duplex Stainless Steels Under Cathodic Protection. *Corrosion* **2010**, *66*, 115004-115004-13. [[CrossRef](#)]
24. Turnbull, A. Modelling of environment assisted cracking. *Corr. Sci.* **1993**, *34*, 921–960. [[CrossRef](#)]

25. Rahimi, S.; Marrow, T.J. A new method for predicting susceptibility of austenitic stainless steels to intergranular stress corrosion cracking. *Mater. Des.* **2020**, *187*, 108368. [[CrossRef](#)]
26. Mujanović, E.; Zajec, B.; Kosec, T.; Legat, A.; Hönl, S.; Zehethofer, G.; Mori, G. Activation and Repassivation of Stainless Steels in Artificial Brines as a Function of pH. *Materials* **2019**, *12*, 3811. [[CrossRef](#)] [[PubMed](#)]
27. Mori, G.; Bauernfeind, D. Pitting and crevice corrosion of superaustenitic stainless steels. *Werkst. Korros.* **2004**, *55*, 164–173. [[CrossRef](#)]
28. Shen, S.; Song, X.; Li, Q.; Li, X.; Zhu, R.; Yang, G. A study on stress corrosion cracking and hydrogen embrittlement of Jethete M152 martensitic stainless steel. *Mater. Sci. Eng. A* **2019**, *740–741*, 243–251. [[CrossRef](#)]
29. Kim, C.D.; Wilde, B.E. A Review of the Constant Strain-Rate Stress Corrosion Cracking Test. In *Stress Corrosion Cracking—The Slow Strain-Rate Technique*; Ugiansky, G.M., Payer, J.H., Eds.; ASTM International: West Conshohocken, PA, USA, 1979; ISBN 978-0-8031-0579-9.
30. Herms, E.; Olive, J.M.; Puiggali, M. Hydrogen embrittlement of 316L type stainless steel. *Mater. Sci. Eng. A* **1999**, *272*, 279–283. [[CrossRef](#)]
31. Cihal, V. The influence of nitrogen, phosphorus, sulphur and nickel on the stress corrosion cracking of austenitic FeNiCr alloys. *Corr. Sci.* **1985**, *25*, 815–819. [[CrossRef](#)]
32. Tseng, C.-M.; Tsai, W.-T.; Liou, H.-Y. Effect of nitrogen content on the environmentally-assisted cracking susceptibility of duplex stainless steels. *Metall Mat. Trans. A* **2003**, *34*, 95–103. [[CrossRef](#)]
33. Toppo, A.; Pujar, M.G.; Mallika, C.; Kamachi Mudali, U.; Dayal, R.K. Effect of Nitrogen on Stress Corrosion Behavior of Austenitic Stainless Steels Using Electrochemical Noise Technique. *J. Mater. Eng. Perform* **2015**, *24*, 1140–1149. [[CrossRef](#)]
34. Kranister, W. Chloridinduzierte Spannungsrisskorrosion an hochlegierten austenitischen Stählen. In *Diplomarbeit*; Montanuniversität Leoben: Leoben, Austria, 2009.

Publisher's Note: MDPI stays neutral with regard to jurisdictional claims in published maps and institutional affiliations.



© 2020 by the authors. Licensee MDPI, Basel, Switzerland. This article is an open access article distributed under the terms and conditions of the Creative Commons Attribution (CC BY) license (<http://creativecommons.org/licenses/by/4.0/>).